Energy-dependent angular shifts in the photoelectron momentum distribution for atoms in elliptically polarized laser pulses

Hui Xie,[1] Min Li,[1,*] Siqiang Luo,[1] Yang Li,[1] Yueming Zhou,[1] Wei Cao,[1] and Peixiang Lu[1,2,†]

[1]*School of Physics and Wuhan National Laboratory for Optoelectronics, Huazhong University of Science and Technology, Wuhan 430074, China*

[2]*Laboratory of Optical Information Technology, Wuhan Institute of Technology, Wuhan 430205, China*

(Received 10 November 2017; published 29 December 2017)

We measure the photoelectron momentum distributions from atoms ionized by strong elliptically polarized laser fields at the wavelengths of 400 and 800 nm, respectively. The momentum distributions show distinct angular shifts, which sensitively depend on the electron energy. We find that the deflection angle with respect to the major axis of the laser ellipse decreases with the increase of the electron energy for large ellipticities. This energy-dependent angular shift is well reproduced by both numerical solutions of the time-dependent Schrödinger equation and the classical-trajectory Monte Carlo model. We show that the ionization time delays among the electrons with different energies are responsible for the energy-dependent angular shifts. On the other hand, for small ellipticities, we find the deflection angle increases with increasing the electron energy, which might be caused by electron rescattering in the elliptically polarized fields.

DOI: 10.1103/PhysRevA.96.063421

I. INTRODUCTION

Atoms or molecules exposed in a strong laser pulse can be ionized with releasing an electron wave packet. According to the Keldysh-Faisal-Reiss (KFR) theory [1], two limiting ionization regimes can be distinguished by the Keldysh parameter γ, i.e., the multiphoton ionization and the tunneling ionization. The Keldysh parameter is defined in atomic units as $\gamma = \omega\sqrt{2I_p}/F_0$, where I_p is the ionization potential, F_0 is the field amplitude, and ω is the laser frequency. The tunneling ionization is dominated when the Keldysh parameter is small as compared with unity ($\gamma \ll 1$), while the multiphoton ionization prevails for large Keldysh parameter ($\gamma \gg 1$).

In the past decades, both tunneling and multiphoton ionizations of atoms and molecules have been extensively studied in linearly polarized laser fields. The ionized electron wave packets can trigger many interesting nonlinear strong-field phenomena, such as high-harmonic generation [2–5], above-threshold ionization (ATI) [6–8], and nonsequential double ionization [9–11]. Using those processes, one can image the molecular orbitals and retrieve the ultrafast dynamics of the electrons and the nucleus in molecules [12–16]. Recently, the use of an elliptically polarized laser field has added more dimensions for the study of the strong-field ionization. Because the elliptically polarized laser field provides a rotating electric field within one laser cycle, the photoelectron momentum distribution is dramatically different from that in a linearly polarized laser field. One of the most prominent features is the lack of fourfold symmetry with respect to both major and minor axes of the laser ellipse, which is known as Coulomb asymmetry [17,18]. In an elliptically polarized laser field with a small ellipticity value, the contributions from the direct trajectory and the forward scattering trajectory have been separated in the final momentum distributions [19]. With increasing the laser ellipticity, the rescattering probability decreases. In a near circularly polarized laser field, the rescattering electron is highly suppressed and the direct ionization is dominant [20]. Because the instantaneous ionization time is mapped to the angle of the final momentum in the polarization plane of a near circularly polarized laser pulse, one can study attosecond-resolved electron dynamics from the photoelectron angular distribution. This technique, dubbed attoclock or attosecond angular streaking, has been widely used in strong-field physics [21–28]. Using the attoclock method, the tunneling time delay [22–25] and the position of the tunnel exit [26] are precisely measured. The attoclock method is often based on the measurement of the deviation of the photoelectron distribution maximum from the prediction of the strong-field approximation [1]. This deviation is characterized by an offset angle with respect to the minor axis of the laser ellipse. It has been shown that many effects such as the nonadiabatic effect [28–30], the electron-electron correlation [27], and the multielectron polarization effect [24,31] are crucial for this offset angle. Most previous works measured the offset angle by integrating the ionization rate over the electron energy. Very recently, it was theoretically predicted that the offset angle depended on the ATI order (or the electron energy) [30]. However, the underlying mechanism of the dependence remains unaddressed.

In the present paper, we measure the photoelectron momentum distributions of atoms ionized by strong elliptically polarized laser fields at the wavelengths of 400 and 800 nm, respectively. The photoelectron momentum distributions show clear electron-energy-dependent angular shifts in both multiphoton and tunneling ionization regimes. For larger ellipticities, we find that the deflection angle with respect to the major axis of the laser ellipse decreases as the electron energy increases in both ionization regimes. This observation is reproduced by the numerical solutions of the time-dependent Schrödinger equation (TDSE) and the classical-trajectory Monte Carlo (CTMC) method. Based on the CTMC model, the energy-dependent angular shifts are attributed to the ionization

*mli@hust.edu.cn
†lupeixiang@hust.edu.cn

 ©2017 American Physical Society

time delays among the electrons with different energies in above-threshold ionization. We show that the combined effect of the Coulomb potential and the initial transverse momentum lead to the ionization time delay. We also find that the dependence of the deflection angle on the electron energy shows an opposite tendency for a small ellipticity value in the multiphoton regime, i.e., the deflection angle with respect to the major axis of the laser ellipse increases as the electron energy increases. The possible reason is discussed.

This paper is organized as follows. In Sec. II, the experimental setup and two theoretical methods are described in detail. In Sec. III, we present our main experimental results and simulated results. The energy-dependent angular shift is well reproduced by both TDSE and CTMC models. The underlying mechanism is also discussed. Finally, we give a brief summary of the paper in Sec. IV. Atomic units ($e = m_e = \hbar = 1$) are used throughout unless specified otherwise. e and m_e are the absolute value of the electron charge and the electron mass, respectively.

II. METHODOLOGY

A. Experiment

We use a newly built cold target recoil ion momentum spectroscopy (COLTRIMS) [32] to measure the PMDs. The laser pulses in our experiments are generated from a Ti:sapphire femtosecond laser system with a repetition rate of 5 kHz at the center wavelength of 800 nm. The laser beam is focused into the supersonic atomic beam with a parabolic mirror ($f = 75$ mm) to ionize the atoms. The supersonic atomic beam is produced by supersonic expansion of high-pressure argon gas into vacuum though a nozzle. Then a cone-shaped skimmer is placed behind the nozzle to extract the cooled beam. After the collimation by two pinholes, the atomic beam is ionized by the focused laser pulse. To retrieve the three-dimensional momenta of both the ionized photoelectrons and photoions, a weak uniformed magnetic field about 8.7 G and a weak uniformed electric field about 8.5 V/cm are used to collect the photoelectrons and photoions. The electrons and the ions fly in opposite directions and, respectively, hit the temporal and position-sensitive detectors (RoentDek, Germany). By measuring the time of flights and the positions of the particles on the detectors, the three-dimensional momenta of the electrons and ions are reconstructed. The pressure below 2×10^{-10} mbar is achieved in the main reaction chamber. We use a $\lambda/2$ plate of 800 nm and a broadband wire grid polarizer to control the laser intensity. The elliptically polarized 800-nm laser field is produced by a combination of a $\lambda/2$ plate and a $\lambda/4$ plate of 800 nm at an ellipticity of $\sim$0.75. The laser intensity of 800 nm used in the experiment is estimated to be $\sim 1.6 \times 10^{14}$ W/cm^2, which corresponds to the Keldysh parameter of 1.1 at the ellipticity of $\sim$0.75 for the argon atom. For this Keldysh parameter, the CTMC model, which is based on the tunneling theory [33], can work well. To study the PMDs in the multiphoton regime, we have also used a strong elliptically polarized laser field at the wavelength of 400 nm to ionize the atoms. Because the 400-nm laser field has a large photon energy of 0.114 a.u., the ATI structures can be easily distinguished from the PMDs, enabling us to study the angular shift of each order of ATI. The 400-nm laser pulse is produced by a 300-μm-thick β-barium borate crystal, which is linearly polarized. Then we rotate the fast axis of a $\lambda/2$ plate before a $\lambda/4$ plate of 400 nm to change the ellipticity of the laser pulse from linear to near-circular polarization while keeping the whole laser intensity unchanged. The laser intensity of 400 nm used in our experiment is $\sim 0.6 \times 10^{14}$ W/cm^2. With varying the laser ellipticities, the range of the Keldysh parameter is 3.0–4.2 for the argon atom. Thus, the electrons are mainly ionized by the multiphoton ionization for the 400-nm pulses.

B. Time-dependent Schrödinger equation

We have used a fully quantum method based on solving the TDSE to reproduce the experimental results. We solve the two-dimensional TDSE in length gauge:

$$i\frac{\partial}{\partial t}\psi(\mathbf{r},t) = \left[-\frac{\nabla^2}{2} + V(\mathbf{r}) + \mathbf{r}\cdot\mathbf{F}(t)\right]\psi(\mathbf{r},t), \quad (1)$$

where $\psi(\mathbf{r},t)$ is the time-dependent electron wave function, $\mathbf{r}$ is the position of the electron, and $V(\mathbf{r}) = -1/\sqrt{\mathbf{r}^2 + a^2}$ is the soft-core potential, $a = 0.624$ for the argon atom. The external laser pulse with the ellipticity ε is described by $\mathbf{F}(t)$:

$$\mathbf{F}(t) = F_0\frac{1}{\sqrt{1+\varepsilon^2}}f(t)\cos(\omega_0 t)\hat{\mathbf{z}} - F_0\frac{\varepsilon}{\sqrt{1+\varepsilon^2}}f(t)\sin(\omega_0 t)\hat{\mathbf{x}}, \quad (2)$$

where $\hat{\mathbf{z}}$ is the major axis and $\hat{\mathbf{x}}$ is the minor axis of the laser ellipse. $f(t)$ is a trapezoidal envelope which has ten optical cycles in total with two cycles ramping on and off:

$$f(t) = \begin{cases} \dfrac{t}{2T}, & 0 < t \leqslant 2T \\ 1, & 2T < t \leqslant 8T \\ \dfrac{10T - t}{2T}, & 8T < t \leqslant 10T \end{cases} \quad (3)$$

where T is the period of the laser pulse. At the end of the pulse, the wave function is further propagated for an additional five optical cycles to ensure all the ionized components move away from the core.

To eliminate the reflections of the wave function from the boundary of the configuration space, we split the wave function into two parts using an absorption function [34]:

$$\psi(\mathbf{r},t) = M_s(r,R_b)\psi(\mathbf{r},t) + [1 - M_s(r,R_b)]\psi(\mathbf{r},t) = \psi_{\text{inner}}(\mathbf{r},t) + \psi_{\text{outer}}(\mathbf{r},t). \quad (4)$$

Here, $M_s(r,R_b) = 1 - 1/(1 + e^{-(r-R_b)/\triangle})$ is the absorption function. In the present simulation, we choose $R_b = 150$ a.u. and $\triangle = 8.0$ a.u. ψ_{inner} is the wave function in the inner region ($r < R_b$) and it is propagated under the combined Coulomb and laser fields. ψ_{outer} is the wave function in the outer region ($r > R_b$) and it is propagated in the momentum space under the Volkov Hamiltonian [35]. For the evaluation of photoelectron spectra in particular, only the outer wave

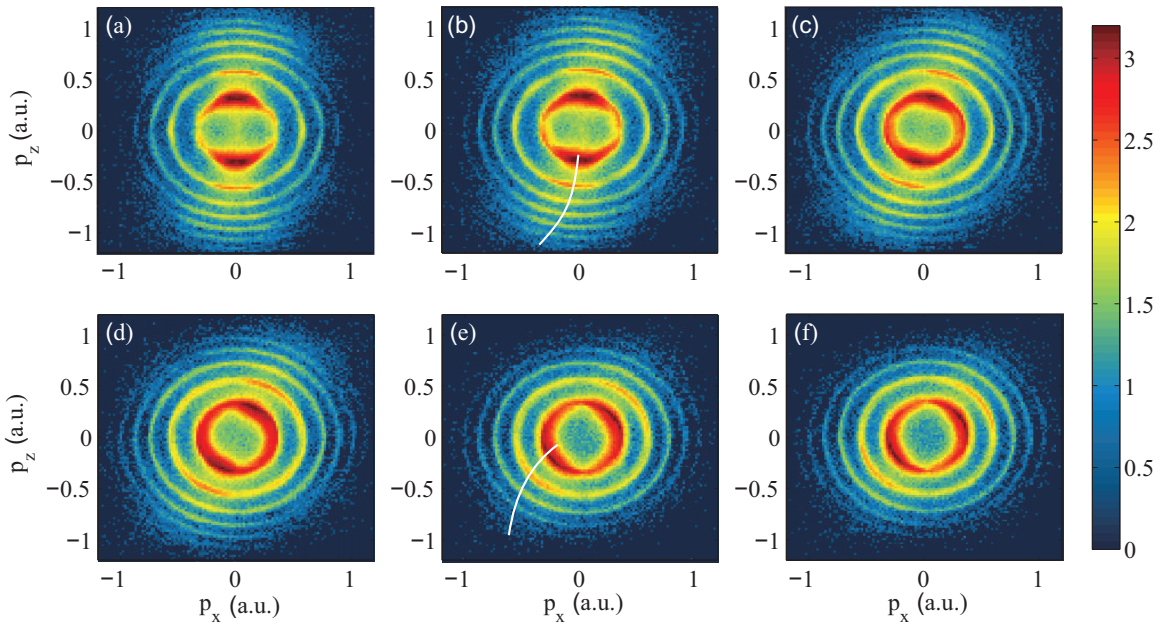

FIG. 1. The measured two-dimensional photoelectron momentum distributions in the polarization plane of argon ionized by 400-nm elliptically polarized laser fields for different ellipticities. The momentum spectra are integrated over $|p_y| < 0.02$ a.u., where p_y is the momentum along the laser propagation direction. The laser ellipticities of (a)–(f) are $\varepsilon = 0$ (linear polarization), 0.16, 0.32, 0.53, 0.75, and 0.87, respectively. p_z and p_x are the momenta along the major and minor axes of the laser ellipse, respectively. The white solid lines in (b) and (e) approximately show the maxima of the photoelectron angular distribution for each order of ATI. The laser intensity is $\sim 6 \times 10^{13}$ W/cm^2.

function is necessary. In each time step, $\psi_{\text{outer}}(\mathbf{r},t)$ is first transformed into momentum space:

$$\tilde{\psi}_{\text{outer}}(\mathbf{p},t) = \iiint \frac{e^{-i[\mathbf{p}+\mathbf{A}(t)]\cdot\mathbf{r}}}{2\pi} \psi_{\text{outer}}(\mathbf{r},t) d^2r, \tag{5}$$

where $\mathbf{A}(t)$ is the vector potential of the laser field and $\tilde{\psi}_{\text{outer}}(\mathbf{p},t)$ is the wave function in momentum space at each time. Then, we propagate the $\tilde{\psi}_{\text{outer}}(\mathbf{p},t)$ from time t to the end of the pulse using

$$\tilde{\psi}^f_{\text{outer}}(\mathbf{p},t) = e^{-i\int_t^\infty \frac{1}{2}[\mathbf{p}+\mathbf{A}(t')]^2 dt'} \tilde{\psi}_{\text{outer}}(\mathbf{p},t), \tag{6}$$

where $\tilde{\psi}^f_{\text{outer}}(\mathbf{p},t)$ is the final wave function in momentum space ionized at time t. Therefore, the final momentum distribution $S(p,\infty)$ is related to the integration of $\tilde{\psi}^f_{\text{outer}}(\mathbf{p},t)$ over t:

$$S(\mathbf{p},\infty) = \left| \int_0^\infty \tilde{\psi}^f_{\text{outer}}(\mathbf{p},t) dt \right|^2. \tag{7}$$

C. Classical-trajectory Monte Carlo model

In order to have a deep insight into the photoelectron momentum distribution, we have also performed a CTMC simulation in an elliptically polarized laser field at the wavelength of 800 nm [19]. In this model, the electron initial position is derived from Landau's effective potential theory [36]. Each electron is weighted by the Ammosov-Delone-Krainov tunneling ionization rate [33]. The weight of each trajectory is given by

$$W(t_0, v_\perp) = W_0(t_0) W_1(v_\perp). \tag{8}$$

Here $W_0(t_0) = |(2I_p)^2/|F(t_0)||^{2/\sqrt{2I_p}-1} \exp[-2(2I_p)^{3/2}/|3F(t_0)|]$ and $W_1(v_\perp) \propto [\sqrt{2I_p}/|F(t_0)|]\exp[\sqrt{2I_p}(v_\perp)^2/|F(t_0)|]$, in which I_p is the ionization potential of argon ($I_p = 15.76$ eV), $v_\perp$ is the initial transverse momentum at the tunnel exit, and t_0 is the ionization time. The elliptically polarized laser field is the same as Eq. (2). After tunneling, the evolution of the electron is governed by the classical Newtonian equation, i.e., $d^2\mathbf{r}(t)/dt^2 = -\mathbf{E}(t) - \nabla \cdot V(\mathbf{r})$. The electron momentum distribution is obtained by summing the electrons with the same momentum weighted by the tunneling ionization rate of Eq. (8).

III. RESULTS AND DISCUSSIONS

We show in Fig. 1 the measured PMDs of argon ionized by elliptically polarized laser pulses from linear to near circular polarizations at the wavelength of 400 nm. Here p_z and p_x are the momenta along the major and minor axes of the laser ellipse, respectively. The PMDs are integrated over $|p_y| < 0.02$ a.u., where p_y is the electron momentum along the laser propagation direction. Because the photon energy of the 400-nm laser field is comparably large (0.114 a.u.), it is easy to distinguish the ringlike ATI structures centered at around zero in the PMDs for all ellipticities. Figure 1(a) shows the PMD in a linearly polarized laser pulse. The PMD is symmetrical with respect to both p_z and p_x axes. Along the laser polarization direction (p_z), all rings show main lobes (maxima) in the PMD. Besides those main lobes in the p_z direction, we can also find some side lobes in the photoelectron angular distributions of the second- and the third-order ATI structures. Those side lobe structures are believed to come from the interferences of the electron wave packets released within a laser cycle [7]. With

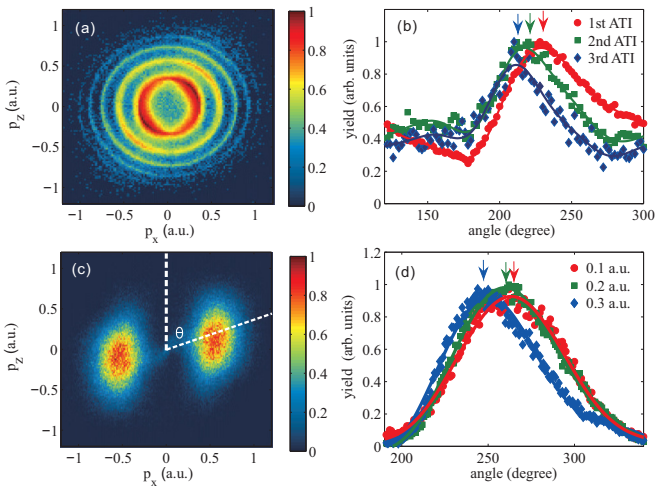

FIG. 2. (a) and (c) show the measured PMDs of Ar using elliptically polarized laser fields with the ellipticity $\varepsilon = 0.75$ at the laser wavelengths of (a) 400 nm and (c) 800 nm, respectively. The PMDs in (a) are the same as Fig. 1(e). (b) The red dots, the dark green squares, and the blue diamonds show the measured angular distribution of the first-, the second-, and the third-order ATIs of (a), respectively. (d) shows the angular distribution of the photoelectrons with the energies of 0.1 a.u. (red dots), 0.2 a.u. (dark green squares), and 0.3 a.u. (blue diamonds) of (c). The arrows in (b) and (d) are used to guide the maximum position of the photoelectron angular distributions. The deflection angle is shown as θ between the two dashed lines in (c).

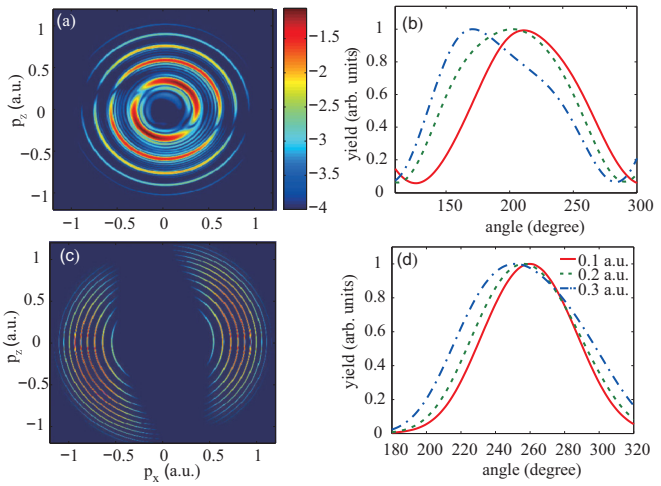

FIG. 3. The same as Fig. 2 but by TDSE calculation. (b) and (d) show the angular distributions of the photoelectrons with the energies of 0.1 a.u. (red solid line), 0.2 a.u. (dark green dashed line), and 0.3 a.u. (blue dash-dotted line) of (a) and (c), respectively.

increasing the laser ellipticities, the main lobes of different orders of ATI in the PMDs are distributed at different angles, as shown in Figs. 1(b)–1(f), revealing distinct angular shifts for the photoelectron distribution maxima. In Figs. 1(b) and 1(c), the PMDs in the elliptically polarized laser fields with small ellipticities of $\varepsilon = 0.16$ and 0.32 are shown, respectively. One can see that the main lobe structures within the ATI rings bend clockwise with the increase of the ATI orders. In contrast, when increasing the ellipticities to $\varepsilon = 0.53, 0.75$, and 0.87, the main lobe structures within the ATI rings bend anticlockwise with the increase of the ATI orders, as shown in Figs. 1(d)–1(f). Therefore, the angular shifts in elliptically polarized laser fields depend sensitively on the electron energy and the laser ellipticity.

We first concentrate on the case of large ellipticity. The PMD of Ar ionized by the 400-nm elliptically polarized laser field at the ellipticity of 0.75 is shown in Fig. 2(a). To further study if the dependence of the angular shift on the electron energy is the same for the multiphoton and tunneling regimes, we have also measured the PMD in an 800-nm elliptically polarized laser field with the ellipticity of 0.75, as shown in Fig. 2(c). The PMD exhibits features which are well known from the previous studies [23–29]. Because the photon energy of the 800-nm laser field is smaller and the laser intensity is higher than the 400-nm laser field, the ringlike ATI structures are blurred by the focal volume effect. To quantitatively describe the energy-dependent angular shifts in the PMDs, we have defined a deflection angle θ in Fig. 2(c) as the deviation of the photoelectron distribution maximum relative to the major axis of the laser ellipse. Note that the deflection angle is different from the usually used offset angle ϑ, which is the angle between the photoelectron distribution maximum and the minor axis of the laser ellipse [28,31]. The relationship between them can be expressed as $\vartheta = 270^\circ - \theta$. For the elliptically polarized laser pulse at the wavelength of 400 nm, the measured photoelectron angular distributions for the first three orders of ATI are shown by red dots (the first-order ATI), dark green squares (the second-order ATI), and blue diamonds (the third-order ATI) in Fig. 2(b). The solid lines in the same color are the fitting curves, using the fourth-order Fourier fitting method. We can find that the peaks of the angular distributions (the deflection angles) of the first-, the second-, and the third-order ATI rings are $\sim$229, $\sim$216, and $\sim$211°, respectively. The deflection angles become smaller with the increase of the electron energy in the elliptically polarized laser pulse at the wavelength of 400 nm. Because the ATI rings are unresolved from the PMD for the 800-nm elliptically polarized laser field, we study the angular shifts at some typical electron energies. In Fig. 2(d), we show the angular distributions for the electron energies of 0.1, 0.2, and 0.3 a.u. Those three energies are very close to the energies of the first-, the second-, and the third-order ATIs in the 400-nm laser pulses. The deflection angles are $\sim$264, $\sim$259, and $\sim$250°, corresponding to the electron energies of 0.1, 0.2, and 0.3 a.u., respectively. The dependence of the deflection angle on the electron energy in an elliptically polarized laser pulse at the wavelength of 800 nm is similar to that in a 400-nm laser pulse.

To reproduce the measured energy-dependent angular shifts, we have numerically solved the TDSE. The TDSE results are shown in Fig. 3. From Figs. 3(a) and 3(c), the ATI structures can be clearly seen in the simulated PMDs of both 400- and 800-nm elliptically polarized laser fields. Figures 3(b) and 3(d) show the angular distributions of photoelectrons with different energies corresponding to Figs. 3(a) and 3(c), respectively. In Fig. 3(b), the deflection angles change from $\sim$215 to $\sim$170° with the increase of the electron energy for

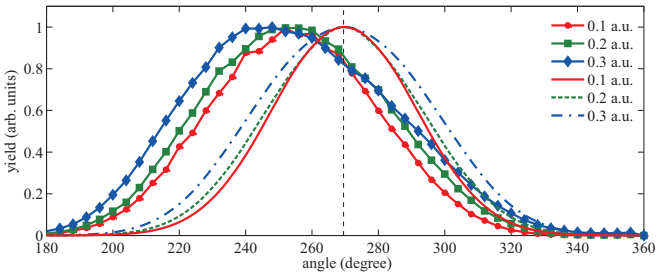

FIG. 4. The normalized angular distributions for the electron energies of 0.1 a.u. (red solid line with dots), 0.2 a.u. (dark green solid line with squares), and 0.3 a.u. (blue solid line with diamonds), in an elliptically polarized laser field at the wavelength of 800 nm ($\varepsilon = 0.75$) using the CTMC method. The red solid line without symbols, the dark green dashed line, and the dash-dotted line are the results without including the effect of the long-range Coulomb potential. The black dashed vertical line shows the angle of 270°, which is the minor axis of the laser ellipse.

the wavelength of 400 nm. For the PMD in the elliptically polarized laser field at the wavelength of 800 nm, the deflection angles change from ∼260 to ∼250° with the increase of the electron energy, as shown in Fig. 3(d). The TDSE results agree qualitatively with the measurements.

Based on the experimental and TDSE results, the deflection angles become smaller with the increase of the electron energy at a large ellipticity for both 800- and 400-nm laser pulses. Because the CTMC model can provide direct interpretation on the underlying mechanism of the energy-dependent angular shift and it can work well for the wavelength of 800 nm, we then use the CTMC model for analysis. The normalized angular distributions calculated by the CTMC model at the wavelength of 800 nm are displayed in Fig. 4 by the solid lines with symbols. The deflection angles are ∼256, ∼252, and ∼246°, corresponding to the electron energies of 0.1, 0.2, and 0.3 a.u., respectively. The deflection angles also become smaller with the increase of photoelectron energy using the CTMC method, which is in good agreement with both the experimental result and the TDSE calculation.

Benefiting from the CTMC model, we can trace the electron trajectories and show the distributions of the ionization times for different electron energies, as shown in Fig. 5(a). We can find that the peaks of the ionization time distributions are different for electrons with different energies. The peaks of the ionization time distributions for the electron energies of 0.1, 0.2, and 0.3 a.u. are $\sim 0.48T$, $\sim 0.49T$, and $\sim 0.51T$, respectively. Comparing the ionization time distributions in Fig. 5(a) with the angular distributions in Fig. 4, we find that the deviations of the deflection angles for different electron energies come from the ionization time delays among them. According to the attoclock principle [22–25], the ionization time is mapped to the angle of the momentum in the polarization plane, i.e., the emission angle is proportional to t_0. Thus the deflection angles with respect to the major axis becomes larger for lower energies.

To further reveal the origin of the ionization time delays among the electrons with different energies, we show the initial transverse momentum distribution with respect to the ionization time using the CTMC method for the electron

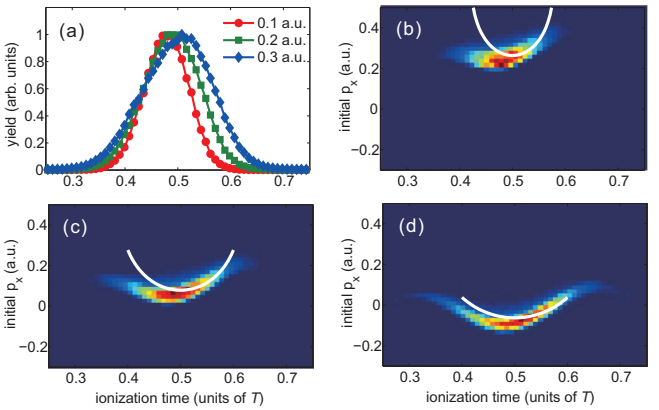

FIG. 5. (a) The ionization time distributions for the electrons with the final energies of 0.1 a.u. (red solid line with dots), 0.2 a.u. (dark green solid line with squares), and 0.3 a.u. (blue solid line with diamonds) using the CTMC method. (b)–(d) show the initial transverse momentum distribution at the tunnel exit with respect to the ionization time for the photoelectrons with different final energies of (b) 0.1 a.u., (c) 0.2 a.u., and (d) 0.3 a.u. The white solid lines in (b)–(d) are the prediction of Eq. (9) without including the Coulomb potential. The laser field is elliptically polarized with the ellipticity of 0.75. The ionization time of $0.5T$ corresponds to the field maximum.

energies of 0.1, 0.2, and 0.3 a.u. in Figs. 5(b)–5(d), respectively. Without considering the effect of the Coulomb potential, the ionization time and the initial transverse momentum should satisfy

$$\left[\frac{F_0}{\omega_0\sqrt{1+\varepsilon^2}}\sin(\omega_0 t_0)\right]^2 + \left[\frac{F_0\varepsilon}{\omega_0\sqrt{1+\varepsilon^2}}\cos(\omega_0 t_0) + v_\perp\right]^2 = 2E_f. \quad (9)$$

Here E_f is the energy of the ionized photoelectron. Equation (9) is given based on the assumption that the electrons are mostly ionized nearby the field maximum.

As shown by the white solid lines in Figs. 5(b)–5(d), the ionization time with respect to the initial transverse momentum predicted by Eq. (9) shows a U-like structure, which is symmetric with respect to $0.5T$ for all energies. Because the ionization rate is the largest at $0.5T$, the ionization time distributions for different energies are all centered by $0.5T$ (the field maximum). As a result, the deflection angles for all electron energies are centered by 270°, as shown by the dashed curves in Fig. 4. Under the influence of the Coulomb potential, the U-like structures appear earlier than the Coulomb-free case. In addition, the U-like structure is tilted, i.e., it shifts downwards for the ionization time before $0.5T$ and shifts upwards for the ionization time after $0.5T$. For such an asymmetric distribution, the maximum ionization rate is determined not only by the ionization time but also by the initial transverse momentum, according to Eq. (8). The photoelectrons ionized with smaller absolute value of the initial transverse momenta have a larger contribution to the final PMD than those with larger absolute value of the initial transverse momenta. For the photoelectrons with the low energy of 0.1 a.u. [Fig. 5(b)], the initial transverse momenta are positive. Thus the ionization time corresponding to the maximum ionization rate shifts to an earlier time than $0.5T$. On

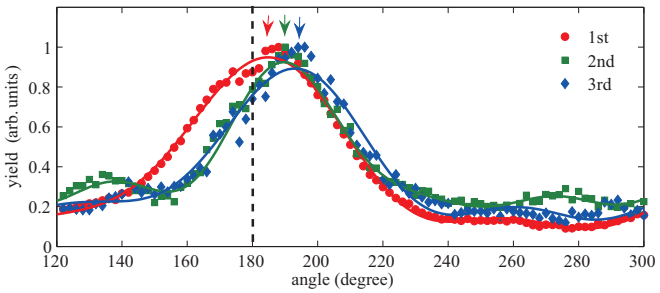

FIG. 6. The measured angular distribution of photoelectrons for the first three orders of ATI of Fig. 1(b). The ellipticity is $\varepsilon = 0.16$. The red dots, the dark green squares, and the blue diamonds show the measured photoelectron angular distributions of the first-, the second-, and the third-order ATIs, respectively. The arrows are used to guide the angles with maximum yield for each order of ATI.

the other hand, for the electrons with the large energy of 0.3 a.u. [Fig. 5(d)], the initial transverse momenta are negative. The ionization time corresponding to the maximum ionization rate shifts to a later time than $0.5T$. Therefore, the combined effects of the Coulomb potential and the initial transverse momentum give rise to the ionization time delays among the electrons with different energies.

In Figs. 2 and 3, we can find that the angular shift for different energies is larger for the 400-nm laser pulse, as compared to the case of the 800-nm laser pulse. This might result from the larger effect of the long-range Coulomb potential on the electron wave packets for the larger Keldysh parameters (shorter laser wavelength) in elliptically polarized laser fields [37,38], which leads to a larger ionization time delay between neighboring ATI orders in the 400-nm fields. In fact, Zipp *et al.* [39] have measured the time delay of the ATI in a two-color laser field with parallel polarizations. Our results also reveal the time delays among the electrons with different energies using elliptically polarized laser fields.

We now turn to the case of small ellipticities. In Fig. 6, we show the measured photoelectron angular distributions of the low-order ATIs of Fig. 1(b). The laser ellipticity is ∼0.16. It can be found that the deflection angles with respect to the major axis of the laser ellipse are ∼186, ∼190, and ∼195° corresponding to the first-, second-, and third-order ATI rings, respectively. The deflection angles become larger with the increase of electron energies, which is different to the case of large ellipticities. As is well known, the formation of the lobe structures in the photoelectron angular distribution of the ATI has been revealed in terms of the interference of the nonscattering and the rescattering trajectories in a linearly polarized laser field [7]. For example, the interference of the forward scattering trajectory with the direct trajectory released from the same quarter of the laser field leads to the spider-leg structure, which shows the maximum, i.e., the main-lobe structure along the laser polarization direction [13]. For elliptically polarized laser fields with small ellipticities, the contribution of the rescattering trajectory is still very important [40–42]. This is because the electron motion induced by the field component along the minor axis of the laser ellipse can be compensated by a small initial transverse momentum of the electron wave packet. It has been shown that for larger Keldysh parameter the rescattering would be more significant [37]. More importantly, the angular distribution of those rescattering electrons is very different with that of the direct electrons, as shown in Ref. [40]. Thus, the energy-dependent angular shifts in elliptically polarized laser fields with small ellipticities might be caused by the electron rescattering process. However, it is difficult to quantitatively investigate the effect of the long-range Coulomb potential on the rescattering trajectory in elliptically polarized laser fields with small ellipticities at the wavelength of 400 nm. It is hoped that the experiment will stimulate theoretical interest.

IV. CONCLUSION

In summary, we have measured the PMDs and the photoelectron angular distributions of argon ionized by strong elliptically polarized laser fields at the wavelengths of 400 and 800 nm, respectively. With increasing the ellipticity of the laser pulse, we found obvious energy-dependent angular shifts in the PMDs. The energy dependences of the angular shifts for the large and low ellipticities are opposite. For large ellipticities, the deflection angle with respect to the major axis of the laser ellipse decreases with the increase of the electron energy for both multiphoton and tunneling ionization regimes. This observation is reproduced by the TDSE and CTMC models. Based on the CTMC calculation, we show that the energy-dependent angular shift comes from the ionization time delay among electrons with different energies. Under the influence of the Coulomb potential, the electron with lower energy is released earlier, thus the deflection angle with respect to the major axis is larger, as compared with the electron with higher energy. We also show that the initial transverse momentum has an important effect on the ionization time delay in above-threshold ionization. In elliptically polarized laser fields with small ellipticities, the angular shift shows an opposite tendency as the electron energy increases, which might result from the electron rescattering effect in the elliptically polarized fields.

ACKNOWLEDGMENTS

This work was supported by the National Natural Science Foundation of China under Grants No. 61405064, No. 11722432, No. 11674116, and No. 11234004 and the Fundamental Research Funds for the Central University, HUST: 2016YXMS012.

[1] L. V. Keldysh, Sov. Phys. JETP **20**, 1307 (1965); F. H. M. Faisal, J. Phys. B **6**, 553 (1973); H. R. Reiss, Phys. Rev. A **22**, 1786 (1980).

[2] P. B. Corkum, Phys. Rev. Lett. **71**, 1994 (1993); M. Hentschel, R. Kienberger, C. Spielmann, G. A. Reider, N. Milosevic, T. Brabec, P. Corkum, U. Heinzmann, M. Drescher, and F. Krausz, Nature (London) **414**, 509 (2001).

[3] J. L. Krause, K. J. Schafer, and K. C. Kulander, Phys. Rev. Lett. **68**, 3535 (1992).

[4] D. Shafir, H. Soifer, B. D. Bruner, M. Dagan, Y. Mairesse, S. Patchkovskii, M. Y. Ivanov, O. Smirnova, and N. Dudovich, Nature (London) **485**, 343 (2012).

[5] F. Wang, W. Liu, L. He, L. Li, B. Wang, X. Zhu, P. Lan, and P. Lu, Phys. Rev. A **96**, 033407 (2017); H. Yuan, F. Li, and H. Long, J. Opt. Soc. Am. B **34**, 2390 (2017); L. Li, Z. Wang, F. Li, and H. Long, Opt. Quant. Electron **49**, 73 (2017).

[6] P. Agostini, F. Fabre, G. Mainfray, G. Petite, and N. K. Rahman, Phys. Rev. Lett. **42**, 1127 (1979).

[7] M. Li, J. W. Geng, Hong Liu, Y. Deng, C. Wu, L. Y. Peng, Q. Gong, and Y. Liu, Phys. Rev. Lett. **112**, 113002 (2014).

[8] Z. Wang, M. Li, Y. Zhou, P. Lan, and P. Lu, Sci. Rep. **7**, 42585 (2017); S. Luo, M. Li, H. Xie, P. Zhang, S. Xu, Y. Li, Y. Zhou, P. Lan, and P. Lu, Phys. Rev. A **96**, 023417 (2017).

[9] D. N. Fittinghoff, P. R. Bolton, B. Chang, and K. C. Kulander, Phys. Rev. Lett. **69**, 2642 (1992).

[10] B. Walker, B. Sheehy, L. F. DiMauro, P. Agostini, K. J. Schafer, and K. C. Kulander, Phys. Rev. Lett. **73**, 1227 (1994).

[11] A. Tong, Y. Zhou, and P. Lu, Opt. Quant. Electron **49**, 77 (2017).

[12] J. Itatani, J. Levesque, D. Zeidler, H. Niikura, H. Pépin, J. C. Kieffer, P. B. Corkum, and D. M. Villeneuve, Nature (London) **432**, 867 (2004); M. Qin and X. Zhu, Opt. Laser Technol. **87**, 79 (2017).

[13] Y. Huismans, A. Rouzée, A. Gijsbertsen, J. H. Jungmann, A. S. Smolkowska, P. S. W. M. Logman, F. Lépine, C. Cauchy, S. Zamith, T. Marchenko, J. M. Bakker, G. Berden, B. Redlich, A. F. G. van der Meer, H. G. Muller, W. Vermin, K. J. Schafer, M. Spanner, M. Y. Ivanov, O. Smirnova, D. Bauer, S. V. Popruzhenko, and M. J. J. Vrakking, Science **331**, 61 (2011).

[14] Y. Zhou, O. I. Tolstikhin, and T. Morishita, Phys. Rev. Lett. **116**, 173001 (2016).

[15] M. He, Y. Zhou, Y. Li, M. Li, and P. Lu, Opt. Quant. Electron. **49**, 232 (2017); M. He, Y. Li, Y. Zhou, M. Li, and P. Lu, Phys. Rev. A **93**, 033406 (2016).

[16] P. Lan, M. Ruhmann, L. He, C. Zhai, F. Wang, X. Zhu, Q. Zhang, Y. Zhou, M. Li, M. Lein, and P. Lu, Phys. Rev. Lett. **119**, 033201 (2017).

[17] M. Bashkansky, P. H. Bucksbaum, and D. W. Schumacher, Phys. Rev. Lett. **60**, 2458 (1988).

[18] S. P. Goreslavski, G. G. Paulus, S. V. Popruzhenko, and N. I. Shvetsov-Shilovski, Phys. Rev. Lett. **93**, 233002 (2004).

[19] M. Li, Y. Liu, H. Liu, Q. Ning, L. Fu, J. Liu, Y. Deng, C. Wu, L.-Y. Peng, and Q. Gong, Phys. Rev. Lett. **111**, 023006 (2013); D. Shafir, H. Soifer, C. Vozzi, A. S. Johnson, A. Hartung, Z. Dube, D. M. Villeneuve, P. B. Corkum, N. Dudovich, and A. Staudte, *ibid.* **111**, 023005 (2013); Y. L. Wang, S. G. Yu, X. Y. Lai, X. J. Liu, and J. Chen, Phys. Rev. A **95**, 063406 (2017).

[20] P. Dietrich, N. H. Burnett, M. Ivanov, and P. B. Corkum, Phys. Rev. A **50**, R3585(R) (1994).

[21] C. P. J. Martiny, M. Abu-samha, and L. B. Madsen, J. Phys. B **42**, 161001 (2009).

[22] P. Eckle, M. Smolarski, P. Schlup, J. Biegert, A. Staudte, M. Schöffler, H. G. Muller, R. Dörner, and U. Keller, Nat. Phys. **4**, 565 (2008).

[23] P. Eckle, A. N. Pfeiffer, C. Cirelli, A. Staudte, R. Dörner, H. G. Muller, M. Büttiker, and U. Keller, Science **322**, 1525 (2008).

[24] L. Torlina, F. Morales, J. Kaushal, I. Ivanov, A. Kheifets, A. Zielinski, A. Scrinzi, H. G. Muller, S. Sukiasyan, M. Ivanov, and O. Smirnova, Nat. Phys. **11**, 503 (2015).

[25] N. Camus, E. Yakaboylu, L. Fechner, M. Klaiber, M. Laux, Y. Mi, K. Z. Hatsagortsyan, T. Pfeifer, C. H. Keitel, and R. Moshammer, Phys. Rev. Lett. **119**, 023201 (2017).

[26] A. N. Pfeiffer, C. Cirelli, M. Smolarski, D. Dimitrovski, M. Abu-samha, L. B. Madsen, and U. Keller, Nat. Phys. **8**, 76 (2012).

[27] A. Emmanouilidou, A. Chen, C. Hofmann, U. Keller, and A. S. Landsman, J. Phys. B **48**, 245602 (2015).

[28] I. A. Ivanov and A. S. Kheifets, Phys. Rev. A. **89**, 021402(R) (2014).

[29] R. Boge, C. Cirelli, A. S. Landsman, S. Heuser, A. Ludwig, J. Maurer, M. Weger, L. Gallmann, and U. Keller, Phys. Rev. Lett. **111**, 103003 (2013); M. Li, M. M. Liu, J. W. Geng, M. Han, X. Sun, Y. Shao, Y. Deng, C. Wu, L. Y. Peng, Q. Gong, and Y. Liu, Phys. Rev. A **95**, 053425 (2017).

[30] M. Murakami and Shih-I Chu, Phys. Rev. A **93**, 023425 (2016).

[31] N. I. Shvetsov-Shilovski, D. Dimitrovski, and L. B. Madsen, Phys. Rev. A **85**, 023428 (2012).

[32] J. Ullrich, R. Moshammer, A. Dorn, R. Dörner, L. Ph. H. Schmidt, and H. Schmidt-Böcking, Rep. Prog. Phys. **66**, 1463 (2003).

[33] M. V. Ammosov, N. B. Delone, and V. P. Krainov, Zh. Eksp. Teor. Fiz. **91**, 2008 (1986) [Sov. Phys. JETP **64**, 1191 (1986)].

[34] Y. Li, M. Li, Y. Zhou, X. Ma, H. Xie, P. Lan, and P. Lu, Opt. Express **25**, 11233 (2017).

[35] D. M. Volkov, Z. Phys. **94**, 250 (1935) [Zh. Eksp. Teor. Fiz. **7**, 1286 (1937)].

[36] L. D. Laudau and E. M. Lifshitz, *Quantum Mechanics* (Pergamon, Oxford, 1977).

[37] M. Li, L. Qin, C. Wu, L.-Y. Peng, Q. Gong, and Y. Liu, Phys. Rev. A **89**, 013422 (2014).

[38] P.-L. He, N. Takemoto, and F. He, Phys. Rev. A **91**, 063413 (2015).

[39] L. J. Zipp, A. Natan, and P. H. Bucksbaum, Optica **1**, 361 (2014).

[40] J. Yu, X. Sun, Y. Shao, M. Li, Q. Gong, and Y. Liu, Phys. Rev. A **92**, 043411 (2015).

[41] X. Y. Lai, C. L. Wang, Y. J. Chen, Z. L. Hu, W. Quan, X. J. Liu, J. Chen, Y. Cheng, Z. Z. Xu, and W. Becker, Phys. Rev. Lett. **110**, 043002 (2013).

[42] G. G. Paulus, F. Zacher, H. Walther, A. Lohr, W. Becker, and M. Kleber, Phys. Rev. Lett. **80**, 484 (1998).